Identification of Lattice Oxygen in Few-Layer Black Phosphorous Exfoliated in Ultrahigh Vacuum and Largely Improved Ambipolar Field-Effect Mobilities by Hydrogenation and Phosphorization

Qingfeng Gui,[†,§] Xiaobin Zhu,[†,§] Lizhe Liu,*[,†] Zhen-Yu Jia,[†] Ye-Heng Song,[†] Shao-Chun Li,[†] Paul K. Chu,[‡] and Xinglong Wu*[,†]

[†]Collaborative Innovation Center of Advanced Microstructures, National Laboratory of Solid State Microstructures and Key Laboratory of Modern Acoustics, MOE, Institute of Acoustics, Nanjing University, Nanjing 210093, China

[‡]Department of Physics and Department of Materials Science and Engineering, City University of Hong Kong, Tat Chee Avenue, Kowloon, Hong Kong 210093, China

S *Supporting Information*

ABSTRACT: Black phosphorus (BP) has recently attracted considerable attention due to its unique structure and fascinating optical and electronic properties as well as possible applications in photothermal agents. However, its main drawback is rapid degradation in ambient environments of H_2O and O_2, which has led to much research on the improvement of its stability. Unfortunately, this research has not shown great improvement in carrier mobilities. Here, we perform scanning tunneling microscopy observations of few-layer BP (FLBP) sheets exfoliated in ultrahigh vacuum and reveal, for the first time, the existence of lattice oxygen introduced during crystal growth. As a proof-of-concept application, hydrogenation is conducted to remove the lattice oxygen atoms followed by phosphorization, which repairs the phosphorous vacancies caused by mechanical exfoliation and hydrogenation. The resulting FLBP sheets show high ambipolar field-effect mobilities of 1374 cm^2 V^{-1} s^{-1} for holes and 607 cm^2 V^{-1} s^{-1} for electrons at 2 K. After storage in air for 3 days, the hole and electron mobilities only decrease to 1181 and 518 cm^2 V^{-1} s^{-1}, respectively, and no structural degradation is observed. This work suggests an effective means to improve both the mobility and stability of BP sheets rendering practical application of FLBP sheets possible.

KEYWORDS: *black phosphorus, lattice oxygen, hydrogenation and phosphorization, stability, ambipolar field-effect mobility*
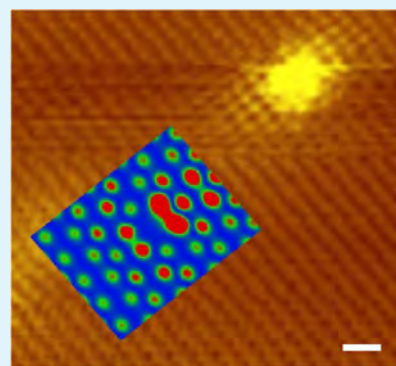
1. INTRODUCTION

Considerable deterioration of surface roughness has been observed on few-layer black phosphorus (FLBP) sheets during 1 h of exfoliation by atomic force microscopy (AFM).[1,2] It was believed that ambient H_2O and O_2 promote PO_x formation and cause degradation of FLBP.[3,4] According to the report by Favron et al.,[5] the rate of oxidation depends on oxygen concentration, light intensity, and energy gap. Even in the dark, oxygen coadsorption with highly polarized water molecules on a black phosphorus (BP) surface also facilitates the electron transfer from BP to oxygen, thus triggering BP oxidation.[6] Moreover, a three-step picture of ambient degradation of BP has shown the generation and dissociation of the superoxide under light and eventual breakdown under the action of water.[7] Hence, surface passivation and encapsulation were commonly used to protect the phosphorene layer.[8−11] For instance, Al_2O_3-encapsulated FLBP can be stable for 8 months,[10] and AlO_x-encapsulated FLBP shows an initial current on−off ratio I_{on}/I_{off} of >10^3 with a hole mobility of 74 cm^2 V^{-1} s^{-1}, which can be maintained for 2 weeks under ambient conditions.[12] In the hexagonal boron nitride-passivated FLBP, the field-effect mobilities of 86 cm^2 V^{-1} s^{-1} for holes and 62 cm^2 V^{-1} s^{-1}

for electrons were observed at 200 K for a duration of 24 h.[13] A benzyl viologen-incorporated FLBP transistor possessed ambipolar properties due to the n-type effect caused by passivation, and the device showed field-effect mobilities of 200 cm^2 V^{-1} s^{-1} for holes and 83 cm^2 V^{-1} s^{-1} for electrons at room temperature for at least 10 days.[14] Aryl diazonium chemistry was also used in FLBP passivation to yield a field-effect mobility for holes of about 100 cm^2 V^{-1} s^{-1} for 2.8 h.[15] BP also shows stable operation under ionic-liquid gating.[16] According to the report by Li et al.,[17] the hole mobility of BP is 984 cm^2 V^{-1} s^{-1} for 10 nm thick phosphorene at 2 K.[17] Nowadays, the boron nitride sandwich technique has led to dramatic improvement of the field-effect mobilities for both holes (3900 cm^2 V^{-1} s^{-1}) and electrons (1600 cm^2 V^{-1} s^{-1}) at T = 1.5 K[18] whereas a graphite gate enabled a carrier Hall mobility of up to 6000 cm^2 V^{-1} s^{-1} in BP thin flakes.[19] A high electron mobility of 2140 cm^2 V^{-1} s^{-1} at low temperature was also acquired by Cu sputtering.[20] However, according to theoretical studies, a much higher field-
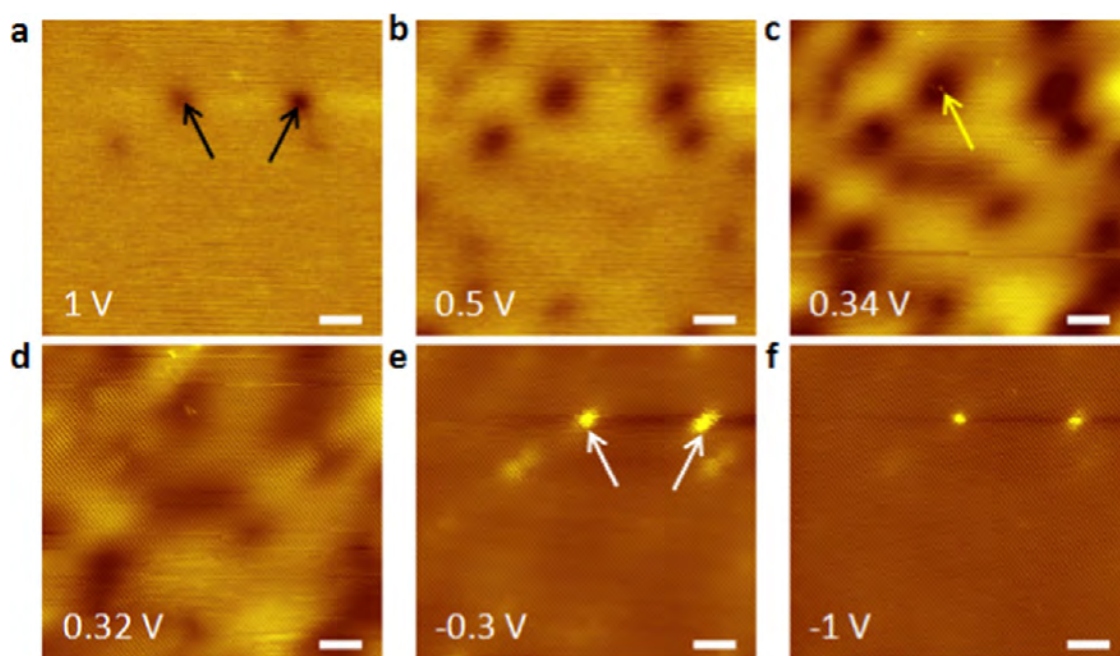
Figure 1. Snapshots of an STM movie taken on the BP (010) surface with spot-like defects under different bias voltages. (a) +1, (b) +0.5, (c) +0.34, (d) +0.32, (e) −0.3, and (f) −1 V. Scale bars: 5 nm. The data are taken at 4.2 K.

effect mobility for holes of about 10 000 cm^2 V^{-1} s^{-1} was predicted for intact phosphorene, and in particular, field-effect mobilities for holes of 6400 and 1580 cm^2 V^{-1} s^{-1} for electrons have been predicted from five-layer black phosphorus sheets.[21] There is concern about the effects of vacancies formed by mechanical exfoliation on the field-effect mobilities, but effective reparation of vacancies via surface passivation/encapsulation has not led to a significant increase in field-effect mobilities.

Herein, scanning tunnel microscopy (STM) is conducted for the first time on FLBP to study the defect types and their correlation with field-effect mobilities. We experimentally and theoretically reveal the existence of lattice oxygen introduced during BP crystal growth. Subsequently, hydrogenation is conducted to remove the lattice oxygen atoms followed by phosphorization, which repairs the phosphorous vacancies caused by mechanical exfoliation and hydrogenation. The resulting FLBP sheets show high ambipolar field-effect mobilities of 1374 cm^2 V^{-1} s^{-1} for holes and 607 cm^2 V^{-1} s^{-1} for electrons at 2 K with good stability in air.

2. EXPERIMENTAL SECTION

2.1. Preparation of FLBP. The single-crystal BP was fabricated in situ according to the procedures reported previously.[22] The FLBP was obtained by cleaving bulk BP crystals by the well-known scotch-tape method.[23] The exfoliated crystals were deposited on SiO$_2$/Si wafers with 300 nm thick SiO$_2$, and the samples were used as gate dielectric materials in the field-effect devices.

2.2. Hydrogenating and Phosphorizing Treatment. The FLBP sheet was treated in a horizontal pipe furnace by chemical vapor deposition. Two milligrams of red phosphorus powder (99.5% from Alfa Aesar) was placed on an alumina boat and inserted into a quartz tube at the front end of a furnace. A rectangular Si substrate (1 cm × 1 cm) with a 300 nm thick surface SiO$_2$ layer was placed downstream in the quartz tube. The distance between the boat and Si substrate was 30 cm. The quartz tube was evacuated to a pressure of 1 × 10^{-5} mbar by a mechanical pump and then purged with Ar (99.99%). In the treatment, the downstream zone was first heated from room temperature to 200 °C in 30 min and maintained at that

temperature for 1.5 h. The upstream zone was heated to 200 °C in 30 min and maintained at that temperature for 45 min after the downstream zone was heated and maintained at 200 °C for 15 min. Afterwards, the furnace was cooled to room temperature slowly. In the initial 75 min, a mixture of Ar (98%) and H$_2$ (2%) was introduced as a carrier gas at a constant flow rate of 100 standard cubic centimeter per minute (SCCM), and in the next 45 min, Ar (99.99%) was introduced as a carrier gas at a constant flow rate of 100 SCCM. The reactions are shown as follows:

$$H_2 + PO_x \rightarrow PH_{2x} + H_2O \tag{1}$$

$$P_y + PH_{2x} \rightarrow P_{vacancy} + PH_3 \tag{2}$$

$$P_{vacancy} + P_y \rightarrow P_{pure} \tag{3}$$

Here, PO$_x$ stands for lattice oxygen defects in the untreated FLBP, and PH$_x$ stands for phosphorus atoms passivated by hydrogen. These phosphorus atoms were previously bound with lattice oxygen before hydrogenation. P$_y$ stands for vapor-phase phosphorus clusters, P$_{vacancy}$ stands for phosphorus vacancies left during hydrogenation and those produced during mechanical exfoliation, and P$_{pure}$ stands for FLBP after hydrogenation and phosphorization.

After the downstream zone reached the set temperature in the initial 45 min, hydrogenation began, in which H$_2$ as the carrier gas reacted with the as-exfoliated FLBP to remove the lattice oxygen, leaving hydrogen-passivated phosphorus vacancies. After the upstream zone reached the set temperature in the following 45 min, phosphorizing treatment began. Red phosphorus precursors produced vapor-phase phosphorus clusters and they mixed with the flowing Ar gas to react with the as-exfoliated FLBP. This removed hydrogen from the passivated phosphorus vacancies and left the phosphorus vacancies to be repaired. At the end of the phosphorizing treatment, all phosphorus vacancies were mended leaving FLBP intact. In our experiments, the FLBP sheets were treated by hydrogenation and phosphorization for 30, 40, 45, and 60 min. We found that a treatment time of 45 min duration produced the best FLBP, which had the least phosphorus clusters and good stability in air.

2.3. Sample Characterization. Raman spectra were acquired using a backscattering geometry on a Jobin-Yvon T64000 triple-grating spectrometer at an excitation wavelength of 514.5 nm. Nuclear magnetic resonance (NMR) spectroscopy was performed on a Bruker

Avance 300 spectrometer at room temperature and the magic angle spinning (MAS) ^{1}H NMR experiments were run at the spinning speed of 10 kHz. X-ray photoelectron spectroscopy (XPS) was conducted on a PHI 5000 Versa Probe. Energy-dispersive X-ray spectroscopy (EDS) was carried out on an electronic differential system with an active area of 10 mm[2]. Scanning tunneling microscopy (STM) was performed on a Unisoku LT-STM 1600 at 4.2 K in the constant current mode under ultrahigh vacuum (UHV) with a base pressure of 1×10^{-10} Torr. The calibration of the tip was done prior and after the measurement with highly oriented pyrolytic graphite. As for STM analysis, the FLBP samples were mechanically exfoliated with a process described as follows: a BP crystal is fixed on a steel pillar and is sent to an UHV chamber. Then, the pillar is knocked out by the cleavage apparatus, carrying off the layered BP below and leaving FLBP sheets with the freshly cleaved surface followed by analysis under UHV with a base pressure of 1×10^{-10} Torr. For atomic force microscopy (AFM) analysis, the FLBP samples were exfoliated in a glove box (filled with 99.99% Ar with atmospheric pressure). The FLBP samples were preserved in laboratory conditions (28.9 °C and 56% relative humidity (RH)) for stability evolution. AFM was conducted on a NanoScope IV NS4-1 instrument. The AFM observations were conducted under a laboratory environment with atmospheric pressure. Here, we would like to point out that as STM observation needs rather high surface planeness, possible cluster deposition introduced by hydrogenation and phosphorization and remarkable degradation in untreated FLBP would make the STM observation impossible. In addition, STM observation also only shows a very small region. Hence, it is more appropriate to judge the sample stability after treatment by AFM, as reported previously. To get an overall observation of the whole FLBP, a larger scale bar of 2 or 5 μm was adopted in our AFM observations.

2.4. Field-Effect Transistor (FET) Device Section. *2.4.1. FET-Device Measurement.* Schematic of the device structure and the optical device image of the FLBP FET are shown in Figure S1, Supporting Information. Contacts were deposited on both sides of a selected FLBP sheet by electron-beam lithography. The Cr/Au electrodes were fabricated by thermal evaporation of 4 nm Cr and 60 nm Au followed by standard lift-off in removing PG. The two-terminal drain current modulation against back-gate voltage (V_g) was measured. The transfer curves were obtained on a Cryomagnetics' C-Mag Vari-9 MGSH-PT system and Keithley 2450.

First-principles density functional theory (DFT) calculations can be found in the Theoretical Section of the Supporting Information.

3. RESULTS AND DISCUSSION

Figure 1 shows the experimental STM images of the surface of a representative (010) BP sheet mechanically exfoliated at UHV (10^{-10} Torr) to avoid impurities under ambient conditions. In contrast to the flat surface on the intact BP at atomic scale (Figure S2, Supporting Information), some dark and white spots are observed. These defect spots are at nanoscale and show clear image evolution with applied bias voltage. If we resolve these spots at atomic scale, as shown in Figure 2, the spot image is obviously diffusive occupying a region of several nanometers due to the extended nature of the defect state wavefunctions.[24] Thus, it is appropriate to observe these defect images at nanoscale. In Figure 1a,b, as the bias voltage is decreased from +1 to +0.34 V, these dark spots become larger (black arrows) and at +0.34 V, a small bright spot emerges at the center of the dark spot (Figure 1c). When the voltage is reduced to +0.32 V (Figure 1d), the dark spots appear more shallow and the boundaries become vague. When the bias is reduced to −0.3 V, the dark spots turn into bright spots (Figure 1e), and finally the bright spots become small at −1 V (Figure 1f).

To determine the defects, density functional theory analysis was performed (details shown in the Calculation Section of Supporting Information). The lattice parameter of the pristine
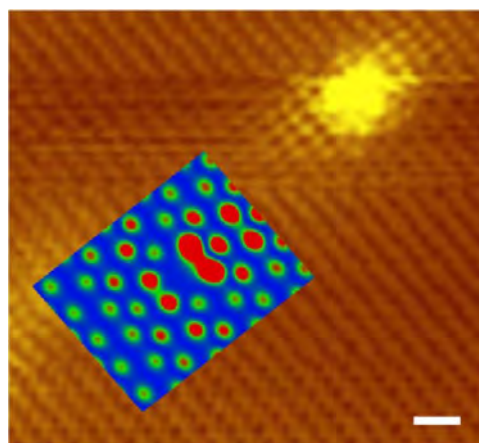

Figure 2. A STM image taken on a representative mechanically exfoliated BP (010) surface with a bright spot-like defect under a bias voltage −0.3 V. Scale bar: 500 pm. The data are taken at 4.2 K. Inset: simulation of STM image of the phosphorene (010) surface with one lattice oxygen at −0.2 V. The size of the DFT image is ∼ 2.3 nm.

BP along the armchair direction was calculated to be 4.64 Å, which is consistent with the previously reported value of 4.58 Å[20] and our experimental value of 4.71 Å (Figure S2), thus validating the calculation. The STM tunneling current in the DFT calculation can be expressed as an integral of the local density of states between the Fermi level E_F and $E_F + eU$[25]

$$I \propto \sum_{n,k} |\phi_n^k(r_0)|^2 \Theta(E_F + eU - E_{n,k}) \Theta(E_{n,k} - E_F)$$

where ϕ_n^k is the states of the surface in the energy interval between E_F and $E_F + eU$, and r_0 is the position of the tip. The image provides information about occupied (unoccupied) states for negative (positive) biases U that modify the Fermi level. To apply a bias voltage to the crystal lattice when simulating with DFT, we firstly perform an orbital calculation, then select the STM profile, and finally import the desired bias voltage. The monolayer BP with one lattice oxygen impurity is presented in Figure 3a (defect region indicated by a yellow circle). At a bias voltage of 2 V (Figure 3b), a dark spot appears around the impurity. When the bias voltage is decreased to 1 V, the dark spot becomes larger and some small bright spots appear from the sites (Figure 3c). When it is further reduced to 0.9 V, the dark spots appear more shallow (Figure 3d). At −0.2 V, the dark spots become bright (Figure 3e), and the bright spots become smaller when the bias voltage is decreased to −0.6 V (Figure 3f). The theoretically derived images are in agreement with the series of experimental STM images shown in Figure 1, indicating that the defects in the BP (010) surface probably stem from lattice oxygen atoms introduced during crystal growth. The inset of Figure 2 shows the simulated STM image with sizes close to the defect spot observed in the atomically resolved STM image (main panel). We can clearly see that these simulated STM images are in coincidence with the experimental results.

As phosphorous vacancy defects can easily form during mechanical exfoliation, we theoretically investigated monolayer BP with one phosphorous vacancy, as shown in Figure 3g. At a bias voltage of 2 V, two dark spots appear around the impurity (Figure 3h), and at 1 V, the dark spots are brighter (Figure 3i). At 0.9 V, the bright spots become larger (Figure 2j), and when the bias voltage is decreased to −0.2 and −0.6 V, the bright
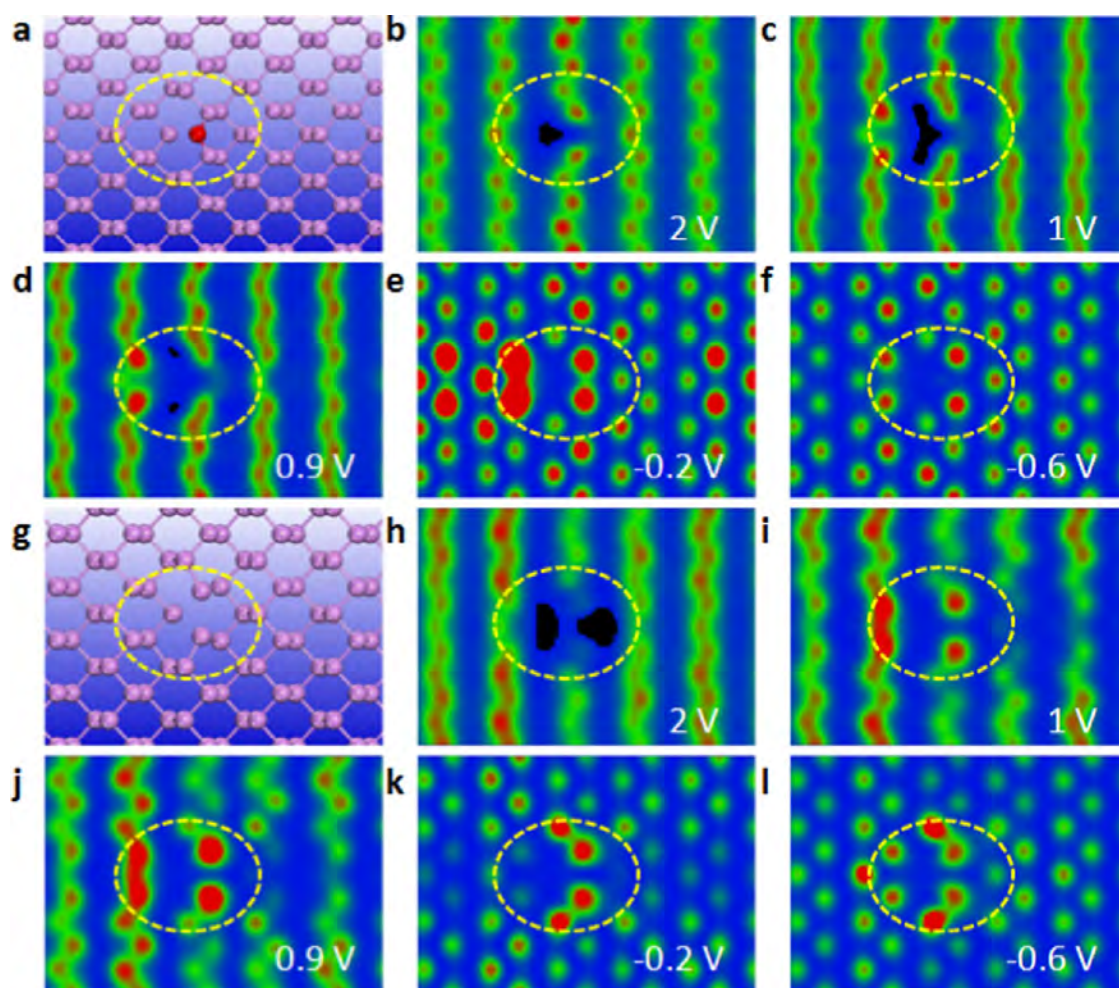
Figure 3. (a) DFT-calculated structure with one lattice oxygen. (b−f) Simulation of STM movies of the phosphorene (010) surface with one lattice oxygen under different bias voltages: (b) 2, (c) 1, (d) 0.9, (e) −0.2, and (f) −0.6 V. (g) DFT-calculated structure with one phosphorus vacancy. (h−l) Simulation of STM movies of the phosphorene (010) surface with one phosphorus vacancy under different bias voltages: (h) 2, (i) 1, (j) 0.9, (k) −0.2, and (l) −0.6 V. The sizes of all DFT images are ∼2.3 nm.

spots become dim (Figure 3k) and do not obviously change (Figure 3l). The phosphorous vacancy images do not match the calculated and experimental STM images of the lattice oxygen defects (Figure 1), and it can thus be inferred that the STM images cannot be caused by phosphorous vacancies produced during mechanical exploitation. To further study the defect types, STM images were theoretically derived from the double lattice oxygen (Figure S3, Supporting Information), double phosphorous vacancy (Figure S4, Supporting Information), a pair of lattice oxygen and phosphorous vacancy (Figure S5, Supporting Information), and one lattice hydrogen (Figure S6, Supporting Information). The results derived from these defects are not consistent with the experimental STM images (Figure 1). Hence, the most probable cause of the defects in the experimental STM images is lattice oxygen, which leads to the frequently observed degradation of as-exfoliated FLBP.

As a proof-of-concept application, we carried out hydrogenation and phosphorization to remove the lattice oxygen and phosphorus vacancy defects produced during mechanical exfoliation. To study the chemical healing processes, AFM was conducted on the FLBP in air (28.9 °C and 56% RH). Figure 4 shows the AFM images of the sample after hydrogenation for 45 min and phosphorization for 45 min (Figure 4a−c for sample 1) and another one that has undergone hydrogenation for 40 min and phosphorization for 40 min (Figure 4d−f for sample 2). The thicknesses of the two FLBP samples are about 7.0 nm (Figure S7, Supporting Information). Sample 1 was kept in air for 30 min before hydrogenation and phosphorization, whereas sample 2 was treated immediately after exfoliation. For sample 1 stored in air for 30 min after exfoliation, a row of clear white spots can be seen from the surface due to slight degradation (arrows in Figure 4a); the root mean square (RMS) for the surface is 2.3 nm. After the treatment, the white spots vanish and only a few phosphorus clusters are observed; the RMS slightly increases to 2.4 nm (Figure 4b). The clusters become larger after sitting in air for 7 days (Figure 4c), indicating that the treatment repairs the slight degradation arising from air exposure. For sample 2, the amount of phosphorus clusters is lower (Figure 4d). The size of the clusters does not change noticeably after 3 days (Figure 4e) and only increases slightly after 7 days (Figure 4f). The FLBP that has undergone hydrogenation and phosphorization exhibits improved morphological stability, and sample 2 is better. The morphological stability was further examined for a longer period of 15 days (Figure S8, Supporting Information). In the initial 7 days, only small degradation is observed (Figure S8a−d). However, from the 11th day, degradation becomes obvious (Figure S8e−g) but slows on the 15th day (Figure
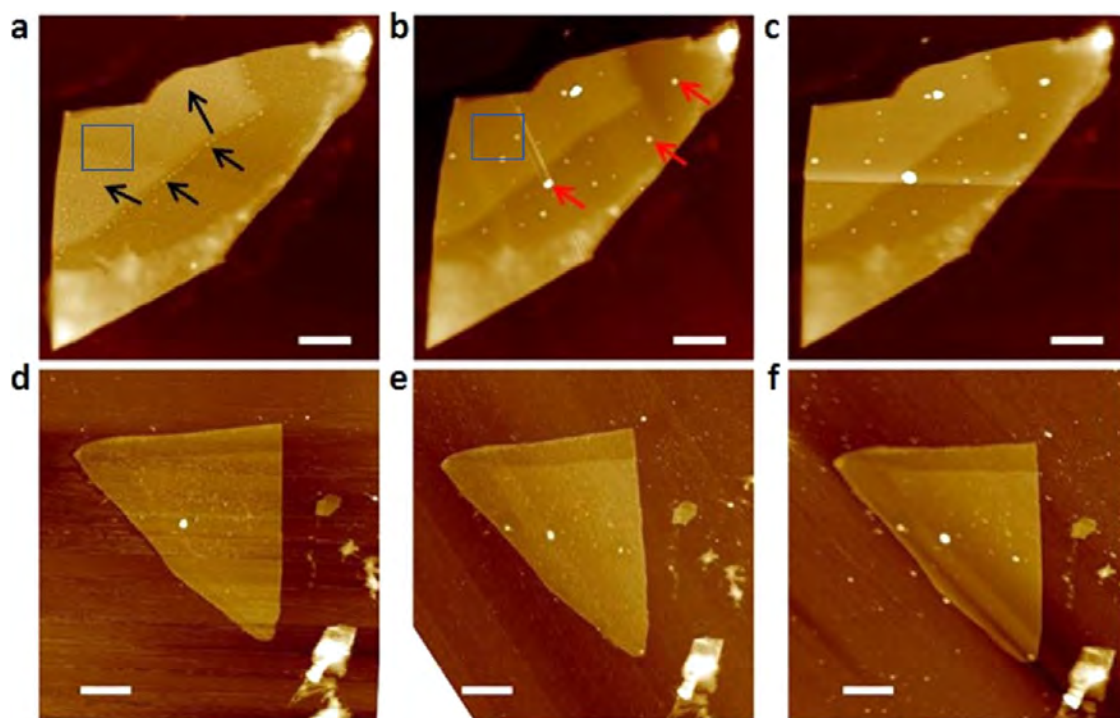
Figure 4. (a) AFM image of the exfoliated sample 1 stored in air for 30 min. (b) AFM image of the as-treated sample 1. (c) AFM image of the treated sample 1 stored in air for 7 days. (d) AFM image of the as-treated sample 2. (e) AFM image of the treated sample 2 stored in air for 3 days. (f) AFM image of the treated sample 2 stored in air for 7 days. The area for RMS measurement is outlined by a rectangular box in (a) and (b). Scale bars: 2 μm.

S8h), indicating that hydrogenation and phosphorization render the FLBP with improved morphological stability for a reasonably long time. In contrast, the surface morphology of the untreated FLBP shows apparent degradation after exposure to air after 3 days with the RMS increasing from 0.5 nm for the as-prepared sample to 7.0 nm (Figure S9a,b, Supporting Information), and it worsens with storage time with an RMS of 13.4 nm (Figure S9c, Supporting Information). As reported previously,[5] the untreated FLBP decomposes into phosphorus oxide species during exposure to ambient water and oxygen, resulting in modified surface morphology and field-effect mobilities.

Nuclear magnetic resonance spectroscopy (Figure 5a) and X-ray photoelectron spectroscopy (Figure 5b) were performed on the FLBP without treatment (called BP-U), after hydrogenation (called BP-H), and after hydrogenation and phosphorization (called BP-HP). The ^{1}HMAS NMR spectrum acquired from BP-U shows a small resonance peak at 9.4 ppm associated with H_3PO_4,[26] indicating that a small amount of degradation has taken place in BP-U.[27] A large resonance peak at 6.2 ppm assigned to H−P bonding is observed from BP-H, suggesting a chemical reaction between hydrogen and BP during hydrogenation. As for BP-HP, a small resonance peak at 10.7 ppm assigned to H_2O is observed, indicating that the treated BP can adsorb water slightly but does not degrade. The XPS spectrum acquired from BP-U shows two peaks at around 130.5 eV (P−P bonding) and 134.2 eV (P−O bonding), revealing oxidation of the as-exfoliated FLBP. After hydrogenation, only the P−P bonding peak is observed, revealing oxide removal, and after hydrogenation and phosphorization, the same is true. Hence, hydrogenation can effectively remove the existing oxide (lattice oxygen) from the as-exfoliated BP. Our Raman results further show that the ^1A_g, B_{2g}, and ^2A_g peaks

of the FLBP respectively appear at 359.6, 438.3, and 465.9 cm^{-1} before and after the treatment (Figure S10, Supporting Information),[28] indicating that there is no structural alteration from additional processing. The 400 cm^{-1} peak characteristic of red phosphorous was not detected, and so the red phosphorus used in the phosphorizing process does not remain in the treated FLBP.[29] To determine the composition of the spots in Figure 4, we measured the energy-dispersive X-ray spectroscopy (EDS) spectra of the FLBP sample and corresponding spots after hydrogenation and phosphorization (Figure S11, Supporting Information). The spectra of both the FLBP and spots are alike with only one peak at 2 keV related to P, indicating that the observed spots are P clusters.

To assess the synergistic effects of hydrogenation and phosphorization, the surface morphology was monitored. The AFM images of BP-H are depicted in Figure S12a,c, Supporting Information. After storage in air for 3 days, surface degradation is obvious, and the RMS increases from 0.95 nm for the as-prepared sample to 3.6 nm after 3 days (Figure S12b,d), and so, hydrogenation, which removes lattice oxygen atoms, cannot maintain the stability due to phosphorus vacancies. Similarly, phosphorization only repairs the phosphorus vacancies but cannot remove lattice oxygen atoms (the RMS increases from 1.5 to 2.0 nm). Our experiments indicate that the combined treatment is necessary to stabilize FLBP. The effects of treatment time on the FLBP structure and stability were explored. After hydrogenation and phosphorization for 30 min each, the FLBP shows a smooth surface (Figure S13a, Supporting Information), but evident degradation occurs after 3 days (Figure S13b) with the RMS increasing from 0.2 to 1.9 nm, indicating that the treatment time is insufficient. After the FLBP has been subjected to hydrogenation and phosphorization for 60 min each, more phosphorous clusters appear from
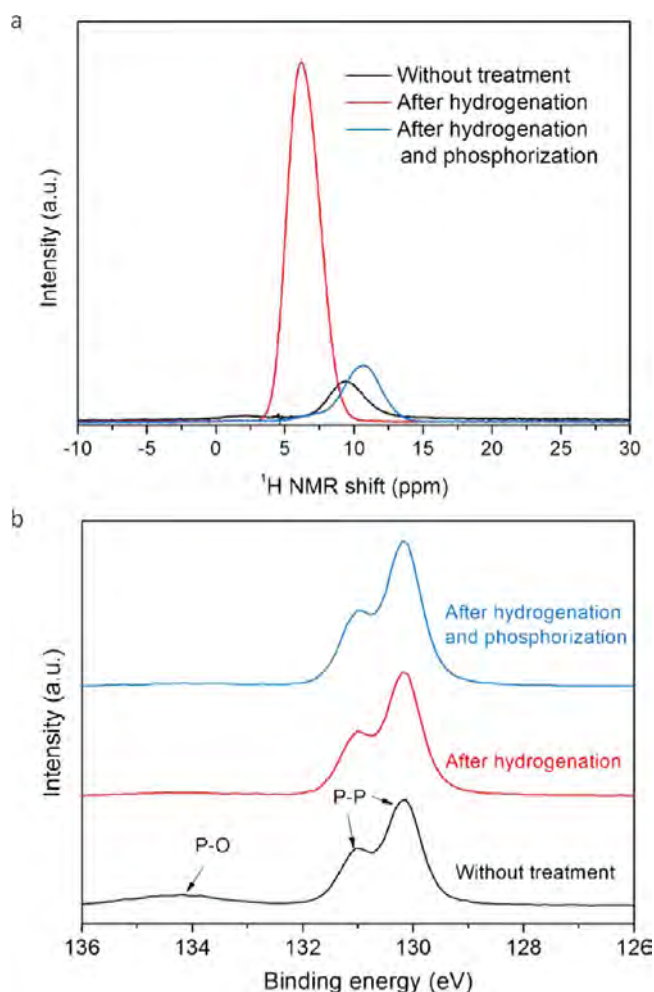
Figure 5. (a) NMR and (b) XPS spectra of FLBP. The black line is for the FLBP without treatment, the red line for the FLBP after hydrogenation, and the blue line for the FLBP after hydrogenation and phosphorization.
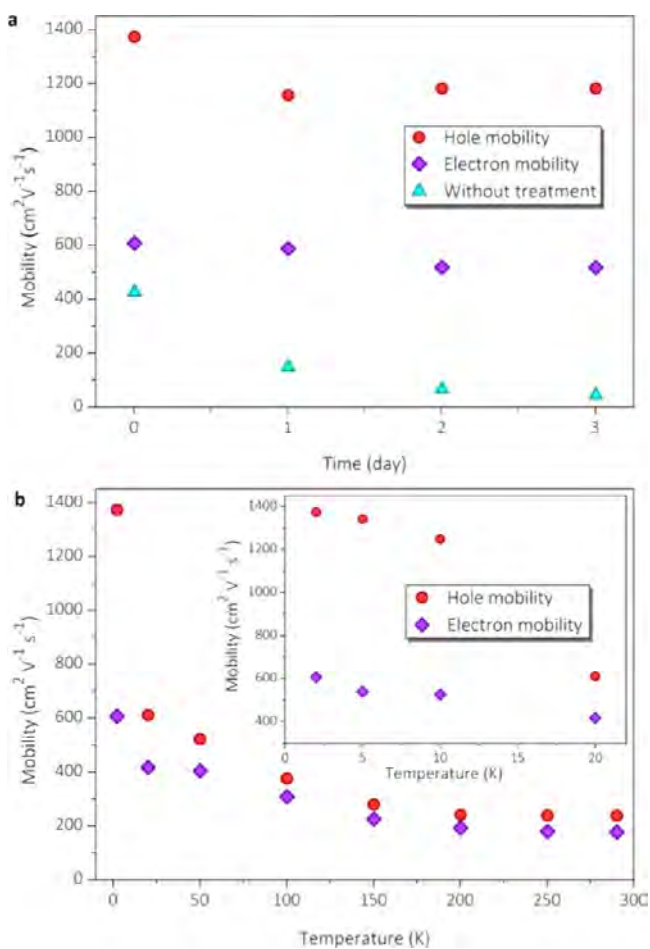

Figure 6. (a) Ambipolar mobilities of the treated FLBP FET as a function of exposure time in air at 2 K. The hole mobility of an untreated FLBP FET is also shown for comparison. (b) Hole and electron mobilities of the treated FLBP FET as a function of temperature in the range from 2 to 290 K. Inset: hole and electron mobilities of the treated FLBP FET as a function of temperature in the range from 2 to 20 K.

the surface (Figure S13c, Supporting Information). The latter treatment reduces surface degradation (Figure S13d, Supporting Information, with the RMS increasing from 2.3 to 2.5 nm) but produces more phosphorous clusters on the surface. This increases carrier scattering, as reported previously,[30] and a proper treatment time is crucial.

The effects of hydrogenation and phosphorization on the electronic properties of the exfoliated FLBP were investigated using the fabricated field-effect transistor. Figure 6a,b shows the mobilities of the treated FLBP FET as functions of exposure time in air and temperature in vacuum, respectively. The FLBP used in the device is about 8 nm thick, and the corresponding transfer curves (I_{ds} against V_g) are presented in Figure S14, Supporting Information. The four curves for different storage times show ambipolar properties and both the electron and hole transport depend upon the polarity of the back-gate voltage. The device shows an on−off ratio of over 10^5 at 2 K for both electron and hole transport in the first day. The ratio diminishes to about 10^4 after 1 day and remains the same after 2 and 3 days. The slope of I_{ds} versus gate voltage V_{gs} is larger on the hole side, indicating a higher field-effect mobility for holes than that for electrons. The field-effect mobility, μ_{FE}, in the linear region is given by

$$\mu_{FE} = \frac{L^2}{C V_{ds}} \frac{dI_{ds}}{dV_{gs}}$$

where L is the length of the channel, V_{ds} is the drain bias, and C is the gate capacitance.[31] The mobilities of the FLBP after the treatment in air within 3 days were calculated and are depicted in Figure 6a. The hole mobility of the treated sample reaches 1374 cm^2 V^{-1} s^{-1} at 2 K. It decreases in the following day and finally stabilizes at 1181 cm^2 V^{-1} s^{-1} in the next 2 days. The high hole mobility reported from the FLBP sheets suggests the important roles of hydrogenation and phosphorization. At a positive gate voltage, the electron mobility reaches 607 cm^2 V^{-1} s^{-1} in the first day. It falls to 587 cm^2 V^{-1} s^{-1} and finally stabilizes at 518 cm^2 V^{-1} s^{-1} in the remaining 2 days, which is much less than that on the hole side. The maintained electron and hole mobilities over time indicate that the chemical process not only improves the stability under ambient conditions, but also introduces excellent ambipolar properties.

To determine the mechanism associated with the ambipolar properties, the band structures of the intact monolayer phosphorene and phosphorene with one lattice oxygen or one phosphorus vacancy were calculated and compared with those in the literature. The details are described in Figure S15,

Supporting Information. The intact phosphorene shows ambipolar properties with the Fermi level in the middle of the bandgap (Figure S15a), which is consistent with the calculated results.[32] For phosphorene with one lattice oxygen defect, the Fermi level moves toward the valence band, indicating p-type characteristics (Figure S15b). When the phosphorus vacancy defect is introduced, p-type conduction still occurs because the Fermi level moves to the top of the valence band (Figure S15c). This implies that although intact phosphorene possesses ambipolar properties, both lattice oxygen and phosphorus vacancies induce p-type characteristics contributing to the p-type conduction experimentally observed from FLBP FETs.[12,13,31] By removing the lattice oxygen and phosphorus vacancy defects using hydrogenation and phosphorizing, the repaired FLBP FETs exhibit ambipolar properties and improved stability. It was noted that introduction of phosphorus clusters to the FLBP surface does not produce significant charge doping because of the equal electronegativity[33] and it is thus not responsible for the enhanced electron mobility. For the device with the untreated FLBP, the p-type behavior is dominant and the field-effect mobility for electrons is much lower than that for holes (Figure 6a). The hole mobility of the device with the untreated FLBP is about 427 cm^2 V^{-1} s^{-1}. It drops to 147 cm^2 V^{-1} s^{-1} in the following day and further decreases to 66 cm^2 V^{-1} s^{-1} after 2 days in air. Finally, it stays at 43 cm^2 V^{-1} s^{-1} in the fourth day. The diminished hole mobility indicates that the FLBP sheet without undergoing hydrogenation and phosphorization degrades rapidly. The field-effect mobility of the device with the treated FLBP as a function of measurement temperature is depicted in Figure 6b. The mobilities decrease from 1374 cm^2 V^{-1} s^{-1} at 2 K to 237 cm^2 V^{-1} s^{-1} at 290 K for holes and from 607 cm^2 V^{-1} s^{-1} at 2 K to 177 cm^2 V^{-1} s^{-1} at 290 K for electrons due to increased scattering with temperature.

4. CONCLUSIONS

Our STM measurements performed in high vacuum and DFT analysis clearly indicate the existence of lattice oxygen atoms in the as-exfoliated FLBP introduced during BP growth. Hydrogenation and phosphorization were conducted to effectively remove the lattice oxygen atoms and repair the phosphorus vacancy defects. The resulting FLBP shows largely improved hole and electron mobilities. This study provides experimental evidence and theoretical insights into ambipolar FLBP with high field-effect mobilities and good stability under ambient conditions.

ASSOCIATED CONTENT

Ⓢ Supporting Information

The Supporting Information is available free of charge on the ACS Publications website at DOI: 10.1021/acsami.7b12469.

> DFT calculations, simulated STM images, DFT-calculated phosphorene structure with various defect structures, AFM images, NMR spectra, XPS spectra, Raman spectra, SEM images, EDS spectra, the transfer curves of a treated FLBP FET as a function of exposure time, and the band structures of FLBP FET (PDF)

AUTHOR INFORMATION

Corresponding Authors

*E-mail: lzliu@nju.edu.cn (L.L.).

*E-mail: hkxlwu@nju.edu.cn. Tel: 86-25-83686303. Fax: 86-25-83595535 (X.W.).

ORCID Ⓘ

Xinglong Wu: 0000-0002-2787-3069

Author Contributions

§Q.G. and X.Z. contributed equally to this work.

Notes

The authors declare no competing financial interest.

ACKNOWLEDGMENTS

REFERENCES

(1) Liu, H.; Neal, A. T.; Zhu, Z.; Luo, Z.; Xu, F. H.; Tomanek, D.; Ye, P. D. Phosphorene: An Unexplored 2D Semiconductor with a High Hole Mobility. *ACS Nano* **2014**, *8*, 4033−4041.

(2) Koenig, S. P.; Doganov, R. A.; Schmidt, H.; Castro Neto, A. H.; Ozyilmaz, B. Electric Field Effect in Ultrathin Black Phosphorus. *Appl. Phys. Lett.* **2014**, *104*, No. 103106.

(3) Yau, S. L.; Moffat, T. P.; Bard, A. J.; Zhang, Z.; Lerner, M. M. STM of the (010) Surface of Orthorhombic Phosphorus. *Chem. Phys. Lett.* **1992**, *198*, 383−388.

(4) Han, C.; Hu, Z. H.; Carvalho, A.; Guo, N.; Zhang, J. L.; Hu, F.; Xiang, D.; Wu, J.; Lei, B.; Wang, L.; Zhang, C.; Neto, A. H. C.; Chen, W. Oxygen Induced Strong Mobility Modulation in Few-Layer Black Phosphorus. *2D Mater.* **2017**, *4*, No. 021007.

(5) Favron, A.; Gaufrès, E.; Fossard, F.; Phaneuf-L'Heureux, A.-L.; Tang, N. Y.-W.; Lévesque, P. L.; Loiseau, A.; Leonelli, R.; Francoeur, S.; Martel, R. Photooxidation and Quantum Confinement Effects in Exfoliated Black Phosphorus. *Nat. Mater.* **2015**, *14*, 826−832.

(6) Hu, Z. H.; Li, Q.; Lei, B.; Zhou, Q. H.; Xiang, D.; Lyu, Z. Y.; Hu, F.; Wang, J. Y.; Ren, Y. J.; Guo, R.; Goki, E.; Wang, L.; Han, C.; Wang, J. L.; Chen, W. Water-Catalyzed Oxidation of Few-Layer Black Phosphorous in a Dark Environment. *Angew. Chem., Int. Ed.* **2017**, *56*, 9131−9135.

(7) Zhou, Q.; Chen, Q.; Tong, Y.; Wang, J. Light-Induced Ambient Degradation of Few-Layer Black Phosphorus: Mechanism and Protection. *Angew. Chem., Int. Ed.* **2016**, *55*, 11437−11441.

(8) Avsar, A.; Vera-Marun, I. J.; Tan, J. Y.; Watanabe, K.; Taniguchi, T.; Castro Neto, A. H.; Ozyilmaz, B. Air Stable Transport in Graphene Contacted, Fully Encapsulated Ultra Thin Black Phosphorus-Based Field-Effect Transistors. *ACS Nano* **2015**, *9*, 4138−4145.

(9) Zhao, Y.; Wang, H.; Huang, H.; Xiao, Q.; Xu, Y.; Guo, Z.; Xie, H.; Shao, J.; Sun, Z.; Han, W.; Yu, X.-F.; Li, P.; Chu, P. K. Surface Coordination of Black Phosphorus for Robust Air and Water Stability. *Angew. Chem., Int. Ed.* **2016**, *55*, 5003−5007.

(10) Illarionov, Y. Y.; Waltl, M.; Rzepa, G.; Kim, J. S.; Kim, S.; Dodabalapur, A.; Akinwande, D.; Grasser, T. Long-Term Stability and Reliability of Black Phosphorus Field-Effect Transistors. *ACS Nano* **2016**, *10*, 9543−9549.

(11) Kim, J.-S.; Liu, Y.; Zhu, W.; Kim, S.; Wu, D.; Tao, L.; Dodabalapur, A.; Lai, K.; Akinwande, D. Toward Air-Stable Multilayer Phosphorene Thin-Films and Transistors. *Sci. Rep.* **2015**, *5*, No. 8989.

(12) Wood, J. D.; Wells, S. A.; Jariwala, D.; Chen, K. S.; Cho, E.; Sangwan, V. K.; Liu, X. L.; Lauhon, L. J.; Marks, T. J.; Hersam, M. C. Effective Passivation of Exfoliated Black Phosphorus Transistors against Ambient Degradation. *Nano Lett.* **2014**, *14*, 6964−6970.

(13) Doganov, R. A.; O'Farrell, E. C. T.; Koenig, S. P.; Yeo, Y. T.; Ziletti, A.; Carvalho, A.; Campbell, D. K.; Coker, D. F.; Watanabe, K.;

Taniguchi, T.; Neto, A. H. C.; Ozyilmaz, B. Transport Properties of Pristine Few-Layer Black Phosphorus by van der Waals Passivation in an Inert Atmosphere. *Nat. Commun.* **2015**, *6*, No. 6647.

(14) Yue, D.; Lee, D.; Jang, Y. D.; Choi, M. S.; Nam, H. J.; Jung, D. Y.; Yoo, W. J. Passivated Ambipolar Black Phosphorus Transistors. *Nanoscale* **2016**, *8*, 12773−12779.

(15) Ryder, C. R.; Wood, J. D.; Wells, S. A.; Yang, Y.; Jariwala, D.; Marks, T. J.; Schatz, G. C.; Hersam, M. C. Covalent Functionalization and Passivation of Exfoliated Black Phosphorus via Aryl Diazonium Chemistry. *Nat. Chem.* **2016**, *8*, 597−602.

(16) Saito, Y.; Iwasa, Y. Ambipolar Insulator-to-Metal Transition in Black Phosphorus by Ionic-Liquid Gating. *ACS Nano* **2015**, *9*, 3192−3198.

(17) Li, L.; Yu, Y.; Ye, G. J.; Ge, Q.; Ou, X.; Wu, H.; Feng, D.; Chen, X. H.; Zhang, Y. Black Phosphorus Field-Effect Transistors. *Nat. Nanotechnol.* **2014**, *9*, 372−377.

(18) Li, L. K.; Ye, G. J.; Tran, V.; Fei, R. X.; Chen, G. R.; Wang, H. C.; Wang, J.; Watanabe, K.; Taniguchi, T.; Yang, L.; Chen, X. H.; Zhang, Y. B. Quantum Oscillations in a Two-Dimensional Electron Gas in Black Phosphorus Thin Films. *Nat. Nanotechnol.* **2015**, *10*, 608−614.

(19) Li, L.; Yang, F.; Ye, G. J.; Zhang, Z.; Zhu, Z.; Lou, W.; Zhou, X.; Li, L.; Watanabe, K.; Taniguchi, T.; Chang, K.; Wang, Y.; Chen, X. H.; Zhang, Y. Quantum Hall Effect in Black Phosphorus Two-Dimensional Electron System. *Nat. Nanotechnol.* **2016**, *11*, 593−597.

(20) Koenig, S. P.; Doganov, R. A.; Seixas, L.; Carvalho, A.; Tan, J. Y.; Watanabe, K.; Taniguchi, T.; Yakovlev, N.; Castro Neto, A. H.; Özyilmaz, B. Electron Doping of Ultrathin Black Phosphorus with Cu Adatoms. *Nano Lett.* **2016**, *16*, 2145−2151.

(21) Qiao, J.; Kong, X.; Hu, Z.-X.; Yang, F.; Ji, W. High-Mobility Transport Anisotropy and Linear Dichroism in Few-Layer Black Phosphorus. *Nat. Commun.* **2014**, *5*, No. 4475.

(22) Köpf, M.; Eckstein, N.; Pfister, D.; Grotz, C.; Krüger, I.; Greiwe, M.; Hansen, T.; Kohlmann, H.; Nilges, T. Access and in situ Growth of Phosphorene-Precursor Black Phosphorus. *J. Cryst. Growth* **2014**, *405*, 6−10.

(23) Meitl, M. A.; Zhu, Z. T.; Kumar, V.; Lee, K. J.; Feng, X.; Huang, Y. Y.; Adesida, I.; Nuzzo, R. G.; Rogers, J. A. Transfer Printing by Kinetic Control of Adhesion to an Elastomeric Stamp. *Nat. Mater.* **2006**, *5*, 33−38.

(24) Wu, X. L.; Xiong, S. J.; Guo, J. H.; Wang, L. L.; Hua, C. Y.; Hou, Y. Y.; Chu, P. K. Ultrathin Amorphous Alumina Nanoparticles with Quantum-Confined Oxygen-Vacancy-Induced Blue Photolumines-cence as Fluorescent Biological Labels. *J. Phys. Chem. C* **2012**, *116*, 2356−2362.

(25) Zollner, K.; Frank, T.; Irmer, S.; Gmitra, M.; Kochan, D.; Fabian, J. Spin-Orbit Coupling in Methyl Functionalized Grapheme. *Phys. Rev. B* **2016**, *93*, No. 045423.

(26) Wang, Y.; Yang, B. C.; Wan, B. S.; Xi, X. K.; Zeng, Z. M.; Liu, E. K.; Wu, G. H.; Liu, Z. Y.; Wang, W. H. Degradation of Black Phosphorus: A Real-Time ^{31}P NMR Study. *2D Mater.* **2016**, *3*, No. 035025.

(27) Chen, P.; Li, J. Y.; Xu, J.; Duan, F. Z.; Deng, F.; Xu, R. R. Synthesis, Structure and NMR Characterization of a New Monomeric Aluminophosphate $[DL-Co(en)_3]_2[Al(HPO_4)_2(H_{1.5}PO_4)_2(H_2PO_4)_2]-(H_3PO_4)_4$ Containing Four Different Types of Monophosphates. *Solid State Sci.* **2009**, *11*, 622−627.

(28) Appalakondaiah, S; Vaitheeswaran, G; Lebègue, S; Christensen, N. E; Svane, A Effect of van der Waals Interactions on the Structural and Elastic Properties of Black Phosphorus. *Phys. Rev. B* **2012**, *86*, No. 035105.

(29) Ramireddy, T.; Xing, T.; Rahman, M. M.; Chen, Y.; Dutercq, Q.; Gunzelmann, D.; Glushenkov, A. M. Phosphorus−Carbon Nanocomposite Anodes for Lithium-Ion and Sodium-Ion Batteries. *J. Mater. Chem. A* **2015**, *3*, 5572−5584.

(30) Xiang, D.; Han, C.; Wu, J.; Zhong, S.; Liu, Y. Y.; Lin, J. D.; Zhang, X. A.; Hu, W. P.; Ozyilmaz, B.; Neto, A. H. C.; Wee, A. T. S.; Chen, W. Surface Transfer Doping Induced Effective Modulation on

Ambipolar Characteristics of Few-Layer Black Phosphorus. *Nat. Commun.* **2015**, *6*, No. 6485.

(31) Fuhrer, M. S.; Hone, J. Measurement of Mobility in Dual-Gated MoS$_2$ Transistors. *Nat. Nanotechnol.* **2013**, *8*, 146−147.

(32) Farooq, M. U.; Hashmi, A.; Hong, J. S. Anisotropic Bias Dependent Transport Property of Defective Phosphorene Layer. *Sci. Rep.* **2015**, *5*, No. 12482.

(33) Bergmann, D.; Hinze, J. Electronegativity and Molecular Properties. *Angew. Chem., Int. Ed.* **1996**, *35*, 150−163.

Identification of Lattice Oxygen in Few-Layer Black Phosphorous Exfoliated in Ultrahigh Vacuum and Largely Improved Ambipolar Field-Effect Mobilities by Hydrogenation and Phosphorization

Qingfeng Gui[1, †], Xiaobin Zhu[1, †], Lizhe Liu[1, *], Zhen-Yu Jia[1], Ye-Heng Song[1], Shao-Chun Li[1], Paul K. Chu[2], and Xinglong Wu[1, *]

[1] Collaborative Innovation Center of Advanced Microstructures, National Laboratory of Solid State Microstructures and Key Laboratory of Modern Acoustics, MOE, Institute of Acoustics, Nanjing University Nanjing, 210093, China

[2] Department of Physics and Department of Materials Science and Engineering, City University of Hong Kong, Tat Chee Avenue, Kowloon, Hong Kong, China

[†]These authors contributed equally to this work.

[*] E-mail: hkxlwu@nju.edu.cn (X.L.W); lzliu@nju.edu.cn (L.Z.L)

Theoretical Section: First-principles density functional theory (DFT) calculations were conducted on the black phosphorus (010) surface using the CASTEP code. A vacuum layer with a thickness of 15 Å was chosen between the phosphorene layers to avoid periodic image interactions. The generalized gradient approximation (GGA) was adopted to describe the exchange correlation. The PBE function was used throughout the calculation presented here and an energy cutoff of 320 eV was used in the plane-wave basis set. The equilibrium geometries were obtained by relaxing the atomic coordinates. The STM images with different defects in phosphorene were calculated using the same DFT parameters used for the pristine phosphorene. To verify the effectiveness of our calculation, a convergence test was taken when simulating the STM images. As shown in **Figure S16**, the STM images were theoretically derived from one lattice oxygen (a, f, k), one phosphorus vacancy (b, g, l), double lattice oxygen (c, h, m), double phosphorous vacancy (d, i, n), and a pair of lattice oxygen and phosphorous vacancy (e, j, o). The first layer shows the STM images with a 6×6 supercell, the second layer shows the STM images with a 7×7 supercell, and the third layer shows the STM images with a 9×9 supercell. These calculation results disclose that the scale of the STM image cannot reach the boundary of the supercell, which confirms that the 7×7 supercell is enough to stimulate the STM features. Therefore, the 7×7 supercell was chosen in this manuscript though the scale bar was different from the experimental pictures.
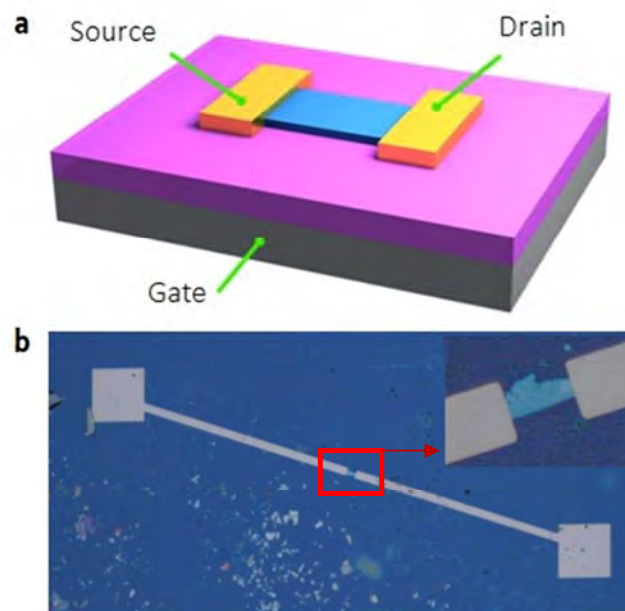
Figure S1. (a) Schematic of the device structure of the FLBP FET. (b) Optical image for the device structure. Inset: the enlarged picture of the center in (b).
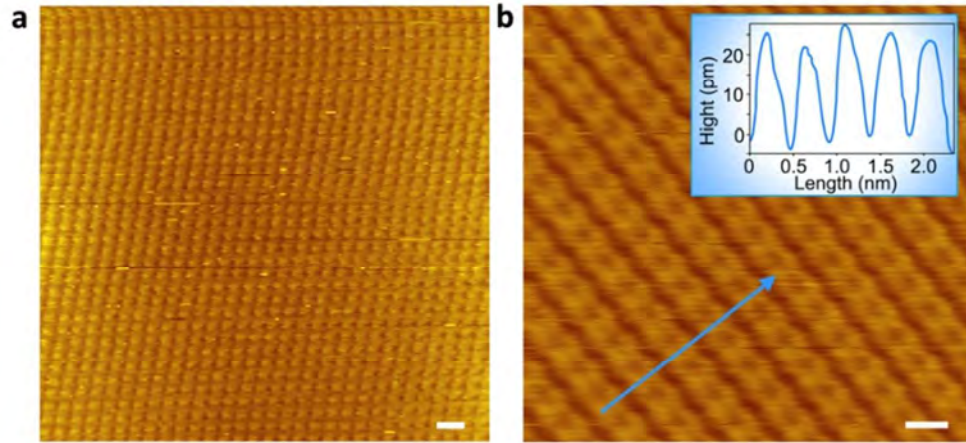
Figure S2. (a) STM images of an intact BP (010) surface in high vacuum. (b) Magnification of picture (a) with distance information in the armchair direction. Inset: height profile extracted along the blue arrow. Scale bars: 500 pm.
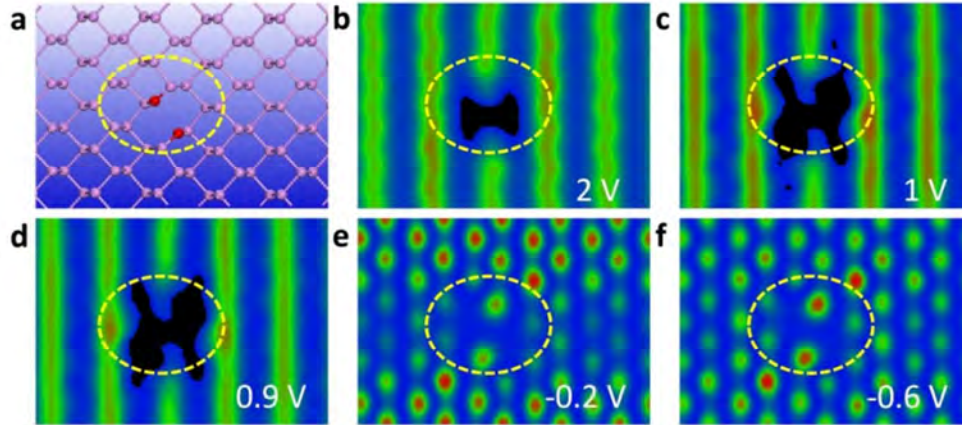
Figure S3. (a) DFT-calculated phosphorene structure with two lattice oxygen atoms, (b-f) Simulation of STM movies of the phosphorene (010) surface with two lattice oxygen atoms at different bias voltages. (b) 2, (c) 1, (d) 0.9, (e) -0.2, and (f) -0.6 V. A dark spot is observed around the impurity at 2 V in (b). When the bias voltage is decreased to 1 V, the dark spot becomes larger in (c). As the bias is further reduced to 0.9 V, the dark spots are unchanged in (d). When the bias voltage reaches -0.2 V, the dark spots totally disappear in (e), and little change is observed when the bias is finally decreased to -0.6 V in (f). These results are not in accordance with the experimental STM images acquired in Figure 1, indicating that the experimentally observed images are not from the double lattice oxygen.
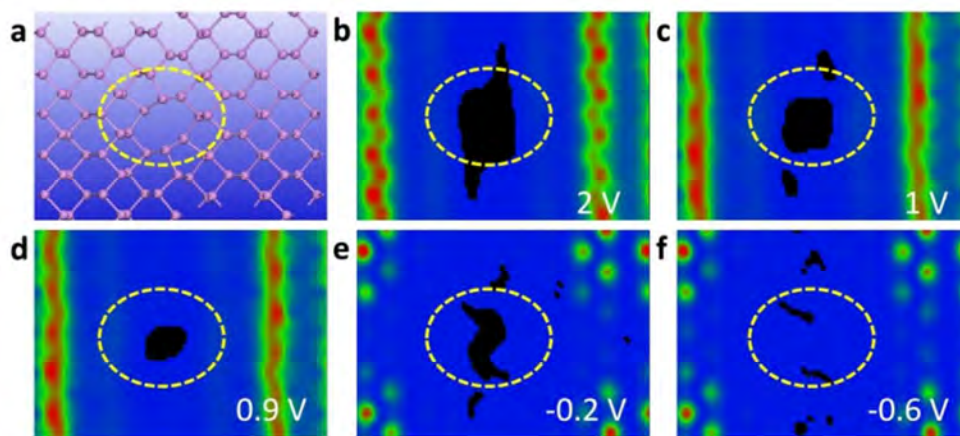
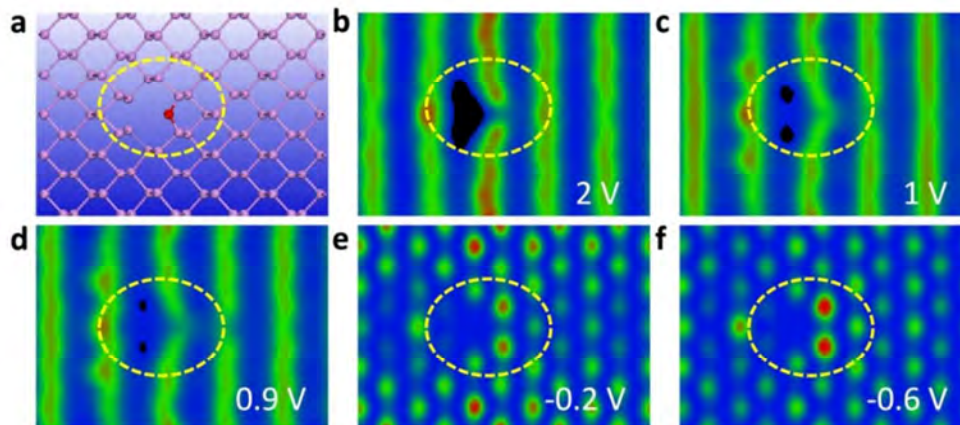**Figure S4.** (a) DFT-calculated phosphorene structure with two phosphorus vacancy defects. (b-f) Simulation of STM movies of the phosphorene (010) surface with two phosphorus vacancy defects at different bias voltages. (b) 2, (c) 1, (d) 0.9, (e) -0.2, and (f) -0.6 V. For the defects, a dark spot is observed around the impurity at the voltage of 2 V in (b). When the bias voltage is decreased to 1 V, the dark spot becomes larger in (c). As it is further reduced to 0.9 V, the dark spot continues to shrink in (d). When the bias voltage reaches -0.2 V, the dark spots change from circular to S shape in (e) and when the bias voltage is finally decreased to -0.6 V, the dark spots becomes minimal in (f). These results are not in accordance with the experimental STM images acquired in Figure 1, indicating that the double phosphorus vacancies also are not the cause of the experimentally observed STM images.

Figure S5. (a) DFT-calculated phosphorene structure with one lattice oxygen and one phosphorus vacancy. (b-f) Simulation of STM movies of the phosphorene (010) surface with one lattice oxygen and one phosphorus vacancy at different bias voltages. (b) 2, (c) 1, (d) 0.9, (e) -0.2 and (f) -0.6 V. A dark spot can be observed around the impurity at a bias of 2 V in (b). The dark spot shrinks into two little dark spots when the bias voltage is decreased to 1 V in (c). As it is further reduced to 0.9 V, the dark spots continue to shrink in (d). When the bias voltage reaches -0.2 V, the dark spots disappear in (e). When the bias voltage is finally decreased to -0.6 V, two bright spots appear at the defect site in (f). These results also are not in accordance with the experimental STM images acquired in Figure 1, indicating that one lattice oxygen and one phosphorus vacancy also are not responsible for the experimentally observed STM images.
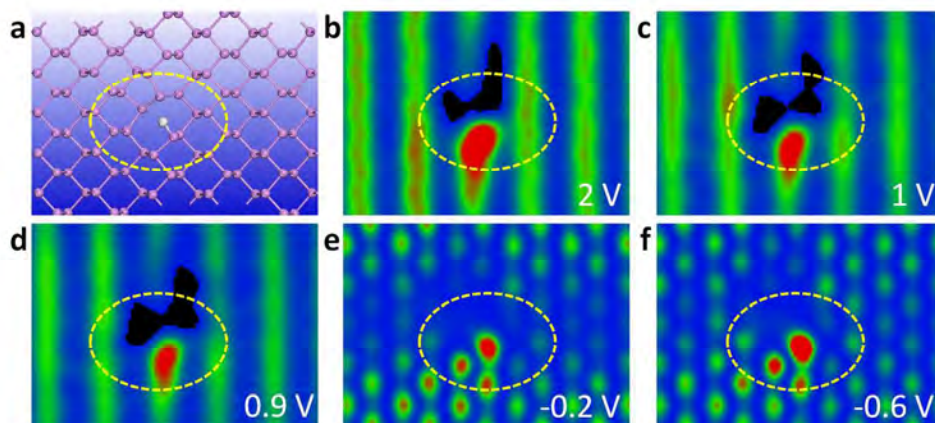
Figure S6. (a) DFT-calculated phosphorene structure with one lattice hydrogen. (b-f) Simulation of STM movies of the phosphorene (010) surface with one lattice hydrogen at different bias voltages. (b) 2, (c) 1, (d) 0.9, (e) -0.2, and (f) -0.6 V. A dark spot and a bright spot can be observed at the impurity site at a bias of 2 V in (b). The dark spot changes little and the bright spot becomes smaller when the bias voltage is decreased to 1 V in (c). As the bias voltage is further reduced to 0.9 V, the dark spot enlarges a little and the bright spot shrinks further in (d). When the bias voltage reaches -0.2 V, the dark spot disappears and the bright spot continues to shrink in (e). When the bias voltage is finally decreased to -0.6 V, the bright spot gets a little brighter at the defect site in (f). These results are not in accordance with the experimental STM images acquired in Figure 1, indicating that one lattice hydrogen is also not responsible for the experimentally observed STM images.
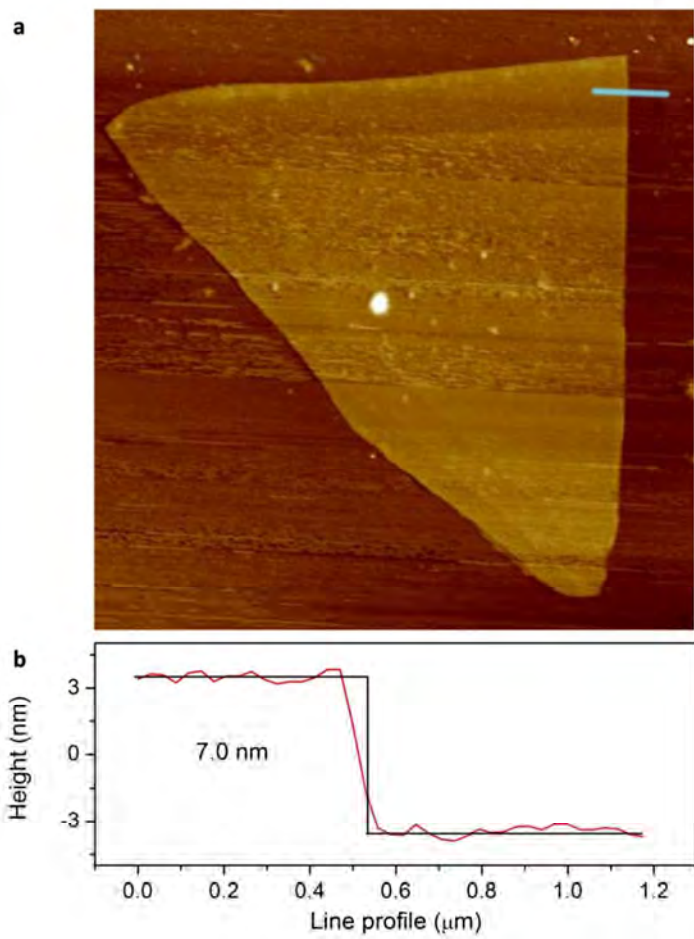
Figure S7. (a) AFM image of a mechanical exfoliated FLBP after treatment (Figure 4d). (b) Height profile of the FLBP extracted along the blue line in (**a**). The height is measured to be about 7.0 nm.
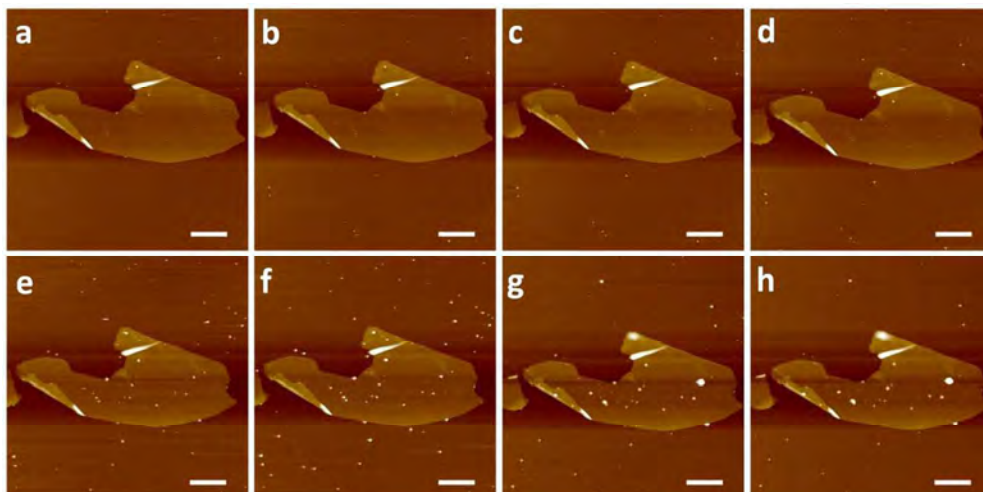
Figure S8. AFM images of a treated FLBP with different storage times in air. (a) 0 (as-treated); (b) 3; (c) 5; (d) 7; (e) 9; (f) 11; (g) 13; (h) 15 days. Scale bars: 5 μm.
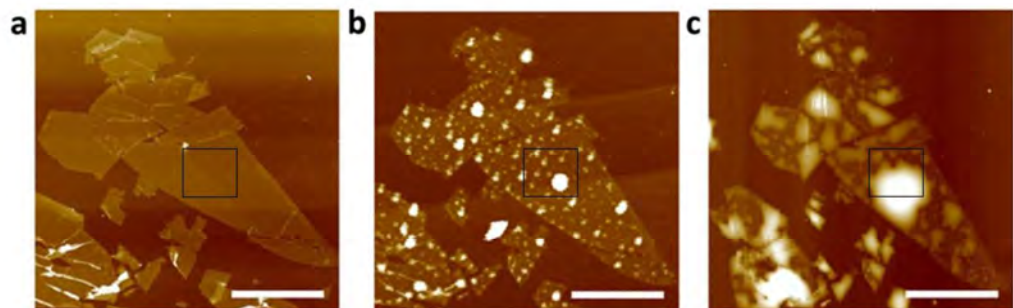
Figure S9. (a) AFM images of a freshly exfoliated untreated FLBP. (b) Same FLBP stored in air for three days. (c) Same FLBP stored in air for seven days. The area for RMS measurement is outlined by the rectangular box. Scale bars: 5 μm.
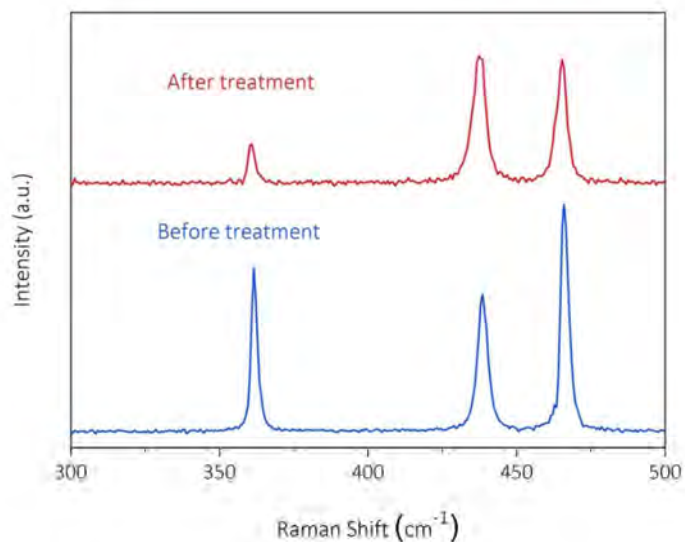
Figure S10. Raman spectra of the FLBP before and after hydrogenation and phosphorization. The red line represents the Raman spectrum of the FLBP after hydrogenation and phosphorization and the blue line represents the Raman spectrum of the FLBP before hydrogenation and phosphorization. Here, we would like to mention that the FLBP is an anisotropic material and exhibits notable anisotropy in Raman spectra as reported previously (*Nat. Commun.* **2014**, 5, 4458). As the Raman measurements of our samples were not taken in the same polarization direction, the Raman spectra were different in intensity for the samples before and after treatment. However, the peak positions remain unchanged, indicating that the structure of the FLBP is not altered from the additional processing.
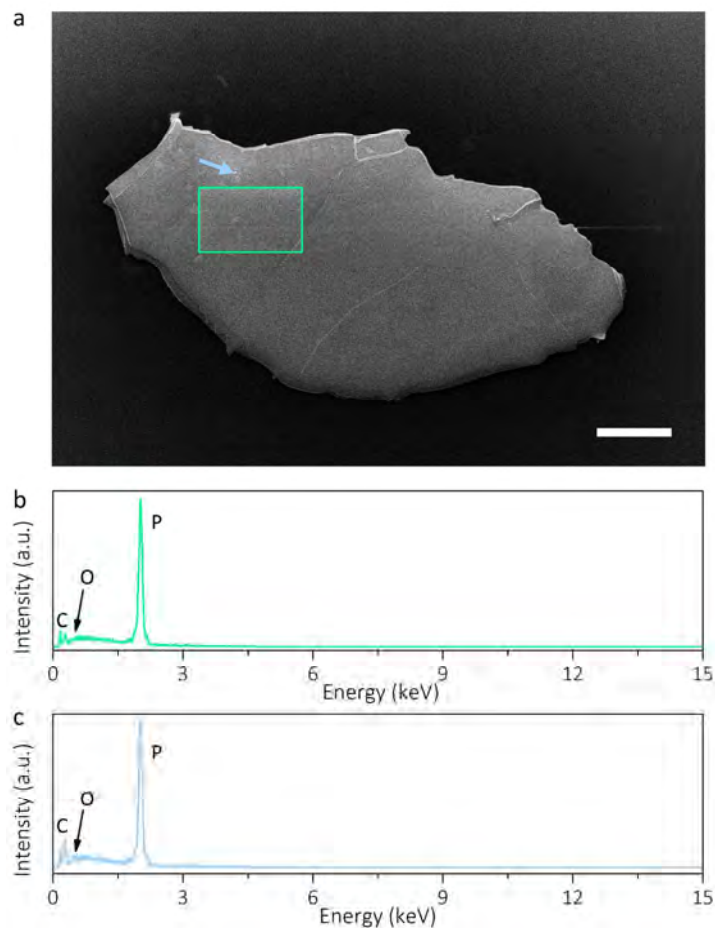
Figure S11. (a) SEM images of a FLBP (010) surface after hydrogenation and phosphorization. The green rectangular box includes a random chosen area of the FLBP surface. The blue arrow points to a spot (P cluster). Scale bar: 50 μm. (b) EDS spectrum of the FLBP within the green rectangular box in (a). (c) EDS spectrum of the spot pointed with the blue arrow in (a).
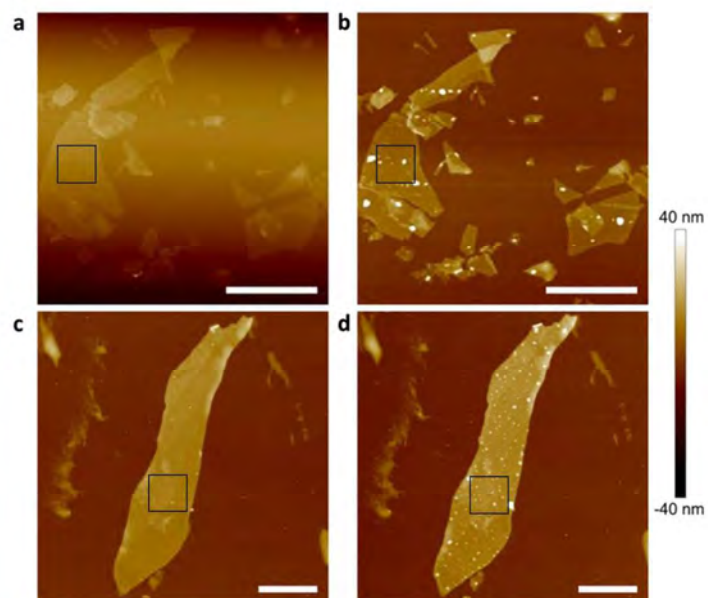
Figure S12. (a) AFM images of representative FLBP sheets after hydrogenation only. (b) Same FLBP stored in air for three days after the treatment. (c) AFM images of representative FLBP sheets after phosphorization only. (d) Same FLBP stored in air for three days after the treatment. The area for RMS measurement is outlined by the rectangular box. Scale bars: 5 μm for (a) and (b); 2 μm for (c) and (d).
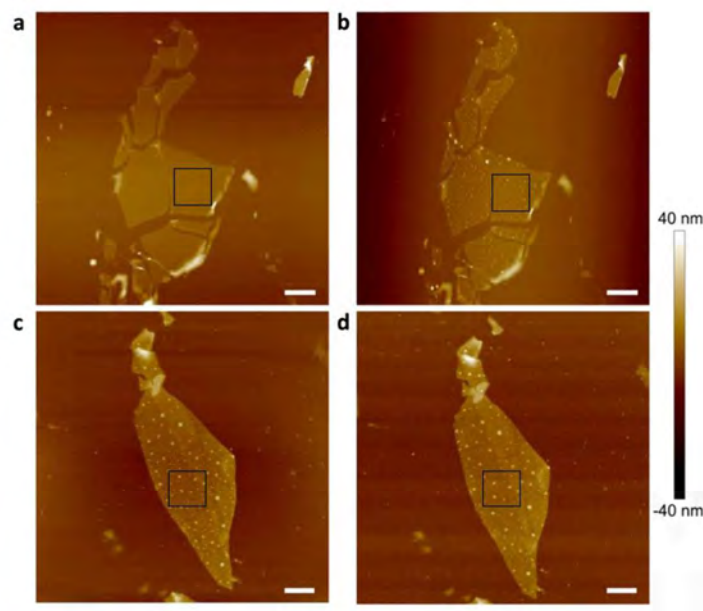
Figure S13. (a) AFM images of representative FLBP sheets hydrogenated and then phosphorized for 30 min, respectively. (b) Same FLBP stored in air for three days after the treatment. (c) AFM images of representative FLBP sheets after hydrogenation and phosphoriation for 60 min, respectively. (d) Same FLBP stored in air for three days after the treatment. The area for RMS measurement is outlined by the rectangular box. Scale bars: 2 μm.
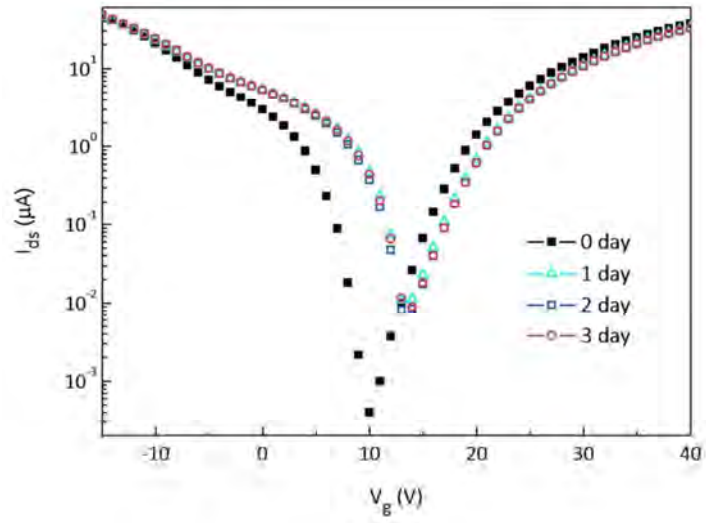
Figure S14. The transfer curves of a treated FLBP FET as a function of exposure time demonstrate strong ambipolar property. The drain current (I_{ds}) is shown as a function of V_g at a temperature of 2 K. A constant source-drain bias of 2 V was applied through the FLBP while V_g was swept from -15 to 40 V.
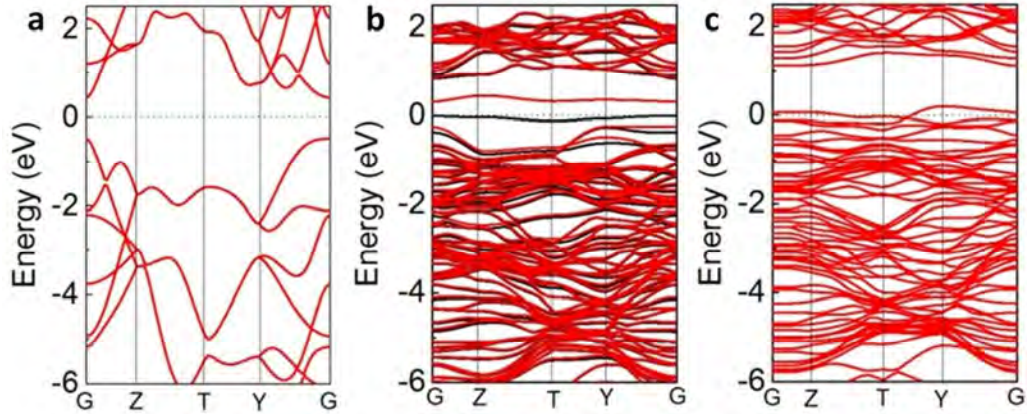
Figure S15. (a) Band structure of the intact monolayer phosphorene. (b) Band structure of the monolayer phosphorene with one lattice oxygen. (c) Band structure of the monolayer phosphorene with one phosphorus vacancy. The Fermi level is set at 0 eV and guided to the eye with a purple dashed line. The intact phosphorene shows ambipolar properties with the Fermi level at the middle of bandgap as shown in (a) which is in good agreement with the previous calculations (Rudenko, A. N., Yuan, S. & Katsnelson, M. I. *Phys. Rev.* B **2015**, 92, 085419; Zhang, R. Q., Wu, X. J. & Yang, J. L. *Nanoscale* **2016**, 8, 4001). With regard to phosphorene with one lattice oxygen, the Fermi level gets into the valence band indicating p-type conduction as shown in (b). When the phosphorus vacancy defect is induced, the p-type conduction appears with the Fermi level moving to the top of valence band as shown in (c). That is, while pure phosphorene exhibits ambipolar properties, both the lattice oxygen and phosphorus vacancy defects induce p-type doping and contribute to p-type conduction in the FLBP FETs as observed experimentally. With the removal of lattice oxygen and phosphorus vacancy defects, the intact FLBP FETs possess ambipolar properties with enhanced hole and electron mobilities.
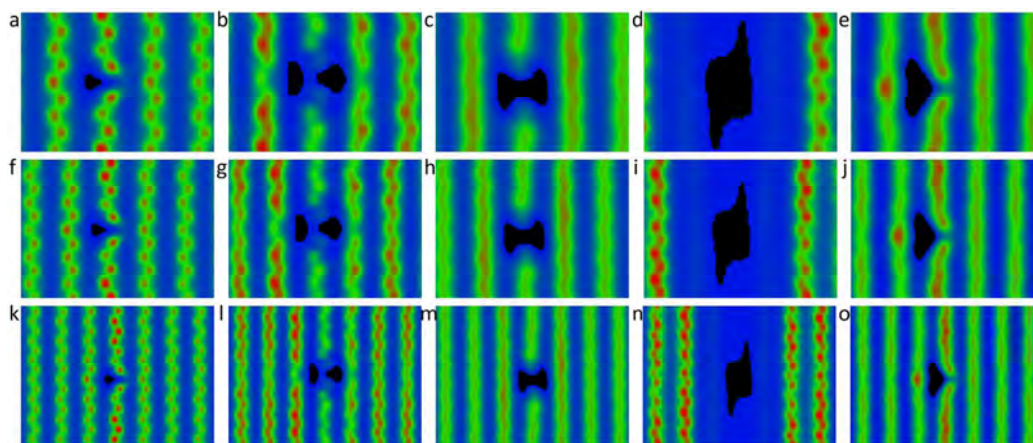
Figure S16. Simulating the STM images derived from one lattice oxygen (a, f, k), one phosphorus vacancy (b, g, l), double lattice oxygen (c, h, m), double phosphorous vacancy (d, i, n), and a pair of lattice oxygen and phosphorous vacancy (e, j, o).